Nano Research 2018, 11(7): 3537–3547
https://doi.org/10.1007/s12274-017-1919-2
Research Article
ISSN 1998-0124
CN 11-5974/O4

Bio-inspired design of hierarchical FeP nanostructure arrays for the hydrogen evolution reaction

Ya Yan[1,5,§], Xue Rong Shi[3,4,§], Mao Miao[2], Ting He[2], Ze Hua Dong[2], Ke Zhan[1], Jun He Yang[1], Bin Zhao[1,5] (✉), and Bao Yu Xia[2,6] (✉)

[1] *School of Materials Science and Engineering, University of Shanghai for Science and Technology, 516 Jungong Road, Yangpu District, Shanghai 200093, China*
[2] *Key laboratory of Material Chemistry for Energy Conversion and Storage (Ministry of Education), Hubei Key Laboratory of Material Chemistry and Service Failure, School of Chemistry and Chemical Engineering, Wuhan National Laboratory for Optoelectronics, Huazhong University of Science and Technology (HUST), 1037 Luoyu Road, Wuhan 430074, China*
[3] *College of Materials Engineering, Shanghai University of Engineering Science, Shanghai 201620, China*
[4] *Institute of Physical Chemistry, University of Innsbruck, Innrain 80-82, Innsbruck A-6020, Austria*
[5] *Shanghai Innovation Institute for Materials, Shanghai 200444, China*
[6] *Shenzhen Institute of Huazhong University of Science and Technology, Shenzhen 518000, China*
[§] *Ya Yan and Xue Rong Shi contributed equally to this work.*

Received: 20 September 2017
Revised: 6 November 2017
Accepted: 11 November 2017

KEYWORDS

bio-inspired
mineralization,
phosphorization,
FeP array,
hydrogen evolution,
density functional theory (DFT) calculations

ABSTRACT

Hierarchical FeP nanoarray films composed of FeP nanopetals were successfully synthesized via a bio-inspired hydrothermal route followed by phosphorization. Glycerol, as a crystal growth modifier, plays a significant role in controlling the morphology and structure of the FeO(OH) precursor during the biomineralization process, while the following transfer and pseudomorphic transformation of the FeO(OH) film successfully give rise to the FeP array film. The as-prepared FeP film electrodes exhibit excellent hydrogen evolution reaction (HER) performance over a wide pH range. Theoretical calculations reveal that the mixed P/Fe termination in the FeP film is responsible for the high catalytic activity of the nanostructured electrodes. This new insight will promote further explorations of efficient metal phosphoride-based catalysts for the HER. More importantly, this study bridges the gap between biological and inorganic self-assembling nanosystems and may open up a new avenue for the preparation of functional nanostructures with application in energy devices.

1 Introduction

Hydrogen is considered as an ideal energy carrier for replacing fossil fuels in the future [1]. Electrocatalytic water splitting offers a promising and environment-friendly approach for the scalable production of

Address correspondence to Bin Zao, zhaobin@usst.edu.cn; Bao Yu Xia, byxia@hust.edu.cn

hydrogen, but requires efficient and inexpensive catalysts to reduce the overpotential of the cathodic hydrogen evolution reaction (HER) [2–5]. To replace noble Pt catalysts, various alternative nanomaterials including metal sulfides/carbides/nitrides have been explored as highly effective electrocatalysts for HER [6–11]. Recently, nanocatalysts such as nanostructured iron phosphide (FeP) have shown high efficiency in the HER process [12, 13]. Various FeP nanostructures have also been reported as HER electrocatalysts, including nanorods, nanoparticles, nanosheets, and their composites [14–16]. It is well known that an ideal catalyst should not only possess a large number of exposed active sites and good electronic conductivity, but the composed electrode architecture should also have a surface structure that favors the rapid removal of the H_2 gas generated [17, 18]. However, only few studies have explored the effect of the morphologies of the FeP nanostructure and the composed electrode on the HER performance. In addition, understanding the activity mechanism and the relationships between the electrocatalytic performance and the components and structure of these systems remains a major challenge.

In the past few decades, a wide variety of biominerals have been shown to have three-dimensional (3D) architectures, usually built by assembling various building blocks such as biopolymers in mild environments [19–21]. Biomineralization events often take place in association with organic molecules through bottom-up processes, and biominerals have been intensively pursued as ideal platforms for the design and fabrication of inorganic nanostructured materials in aqueous systems [22]. Various biomimetic synthetic routes have been developed for manufacturing highly ordered inorganic architectures [23–26]. However, most previous studies focused on alkaline earth metal-based phosphates and carbonates [27, 28]. It would be of high interest to further expand these bio-inspired engineering strategies to the design and synthesis of inorganic and non-biological mineral nanostructures, with potential multidisciplinary applications in electronic and electrochemical energy technologies.

Herein, a FeP array film electrode composed of FeP nanopetal building blocks is prepared through a bio-inspired hydrothermal route followed by a phosphorization process. In the first step, glycerol works as a crystal growth modifier in controlling the morphology and structure of the FeO(OH) film precursor during the biomineralization process, while the following transfer and subsequent pseudomorphic transformation of the FeO(OH) film precursor successfully give rise to the FeP array film electrode. The array film electrode exhibits excellent electrocatalytic HER performance over a wide pH range. Together with theoretical calculations, the present results are also used to formulate a mechanism for the HER activity of the FeP electrode.

2 Results and discussion

2.1 Synthesis and characterization

The fabrication of the hierarchical FeP film electrodes is illustrated in Fig. 1. In the first step, a FeO(OH) array film composed of uniform nanopetals is produced via a bio-inspired hydrothermal route. No FeO(OH) film is observed before adding glycerol during the hydrothermal process, suggesting that glycerol might act as crystal growth modifier and mediate the formation of the FeO(OH) precursor. Afterwards, the FeO(OH) film is carefully transferred to a clean Ti foil which serves as the electrode substrate, and the as-transferred samples are put in an oven at 80 ˚C for 30 min to enhance the contact between FeO(OH) film and Ti foil. The third step involves a pseudomorphic phosphorization reaction converting the supported FeO(OH) films to FeP films under PH_3 atmosphere. The hierarchical FeP electrode with favorable surface structure was thus fabricated by combining bio-inspired

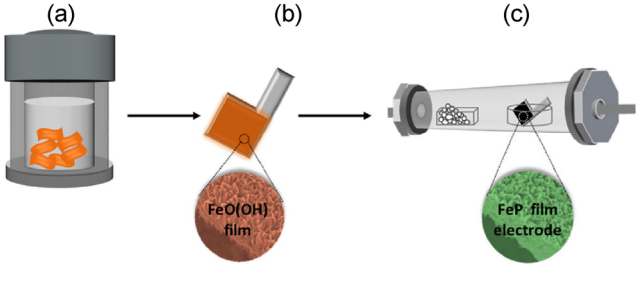

Figure 1 Illustration of the fabrication of hierarchical FeP film electrodes. (a) Bio-inspired hydrothermal growth; (b) transfer of α-FeOOH films; (c) *in situ* phase transformation of α-FeOOH film to hierarchical FeP film electrode.

mineralization and phase transformation processes (Fig. S1 in the Electronic Supplementary Material (ESM)). Ti substrates have been employed in this work, because Ti not only promotes the adhesion of the FeP film, but is also electrochemically inactive in the HER and remains chemically inert during that process.

The crystallographic structure and phase purity of the FeO(OH) film and the phosphidated product were investigated by X-ray diffraction (XRD) (Fig. S2 in the ESM). The as-synthesized iron oxide film exhibits diffraction patterns characteristic of α-phase FeO(OH) (JCPDS no. 29-0713), even though the relative peak intensities do not exactly match the simulated ones. The slight mismatch could be attributed to the preferred orientation [29]. After the solid/gas-phase reaction, the diffraction peaks of the products match those of FeP (JCPDS no. 65-2595), confirming the successful conversion of α-FeO(OH) to FeP after the low-temperature phosphorization process, even though the weak (00*l*) diffraction peaks denote poor crystallinity. The scanning electron microscopy (SEM) images in Fig. 2 clearly show the film morphologies of the as-prepared FeO(OH), consisting of nanoarray structures. The film consists of a large number of uniformly aligned nanopetals, nearly perpendicular to the film plane; some petals even assemble into nanoflowers (Fig. 2(a)). The cross-section SEM images highlight the presence of large numbers of nanopetal building blocks on both sides of the as-obtained FeO(OH) film

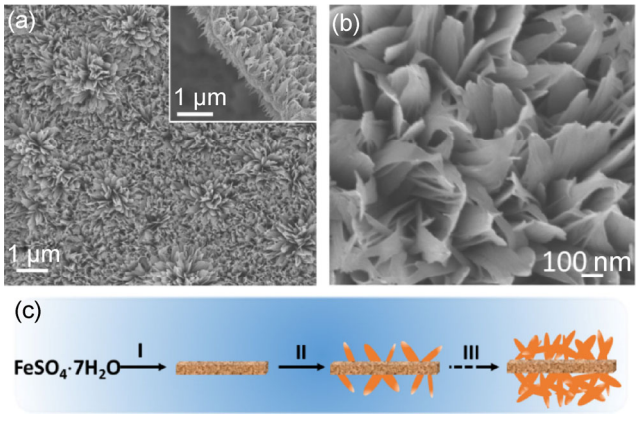

Figure 2 (a) and (b) Field-emission SEM (FESEM) images of FeO(OH) film precursor. The inset in panel (a) shows a cross-section view. (c) Schematic illustration of the formation of the FeO(OH) array films.

(inset of Fig. 2(a)), while the central part of the film is composed of a large amount of nanoparticles tightly stacked on top of each other. This nanoparticle layer could act as the growth substrate for the additional formation of isolated nanopetals. Figure 2(b) displays a high-magnification SEM image of the α-FeO(OH) nanopetals, which reveals that the petals have a very smooth surface, along with a thickness of 5–10 nm and a lateral size of 200–300 nm. Similar structures have also been reported for other compounds such as NiO [30], WO_3 [31], MoS_2 [17], and some layered double hydroxides (LDHs) [32]. However, the previously reported thin array films were usually grown directly on solid substrates or supports, rather than by a template-free hydrothermal process.

We then investigated the influence of the glycerol concentration on the product morphology (Fig. S3 in the ESM). Decreasing the glycerol/water volume ratio to 1:7 results in the formation of films composed of vertically aligned nanorods on both sides (Figs. S3(a) and S3(b) in the ESM). On the other hand, when the volume ratio is increased to 1:1, films can only be obtained at the interface of the solution, and the nanopetals only grow on one side of the film (Figs. S3(e) and S3(f) in the ESM). This could be due to the relatively high buoyancy of the produced film resulting from the enhanced solvent density, which causes the initially formed particles to assemble at the air-solution interface, serving as growth substrate for the further formation of nanopetals on the solution surface.

The growth process of FeO(OH) films during the hydrothermal reaction was studied by time-dependent experiments. At an early reaction stage (4 h), a large amount of FeO(OH) nanoparticles can be observed in the sample (Figs. S4(a) and S4(b) in the ESM). When the incubation time is increased to 8 h, nanoparticle layers are formed and act as growth substrates for isolated nanopetals (Figs. S4(c) and S4(d) in the ESM). As the reaction proceeds, both the number and density of nanopetals increase, and some flower-like structures are also observed (marked as white circles in Figs. S4(e) and S4(f) in the ESM). Thereafter, well-defined FeO(OH) films composed of vertically aligned nanopetals are formed after 12 h of reaction (Figs. 2(a) and 2(b)). Based on these findings, a potential growth mechanism of the FeO(OH) array films is shown in

Fig. 2(c). First, FeO(OH) nanoparticles stack together to form a thin layer, which serves as substrate for the subsequent growth of isolated nanopetals and flower-like structures. As the reaction proceeds, the structure, size, and density of the nanounits increase, and well-defined FeO(OH) array films composed of nanopetals are eventually obtained at longer reaction times.

Surprisingly, the two-dimensional array remains intact after the phosphidation process (Fig. 3(a) and inset), and exhibits a nanoporous structure with holes of size ranging from 50 to 200 nm among the petals (Fig. 3(b)). Compared with the FeO(OH) films, the obtained FeP films have a similar larger lateral size and film thickness, with a slightly adjacent due to the sintering process. The energy dispersive X-ray (EDX) spectrum gives a Fe/P ratio of 1:1.08 for the FeP films,

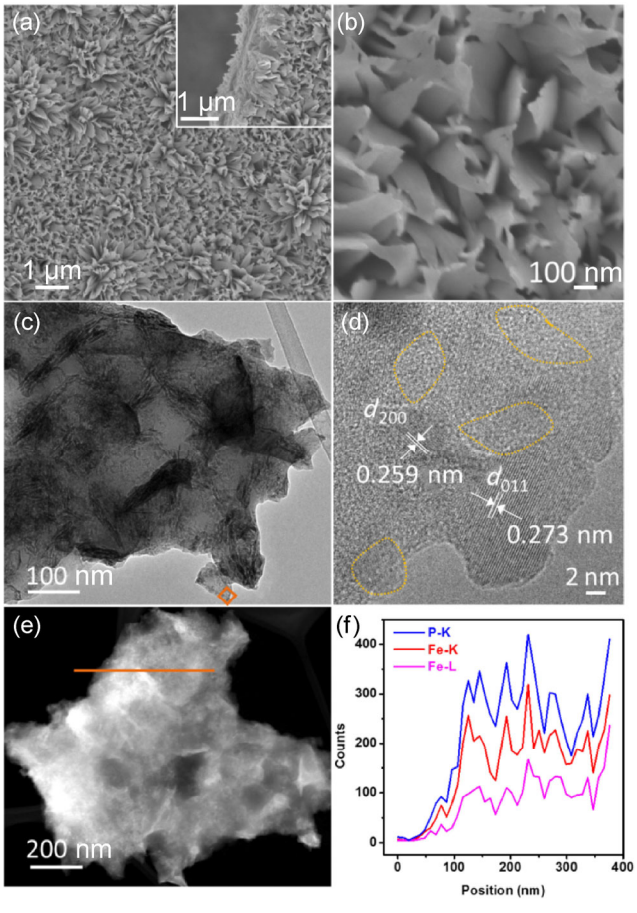

Figure 3 (a) and (b) FESEM images of hierarchical FeP film. The inset in panel (a) shows a cross-section view. (c) TEM image of FeP nanopetals scraped off the film electrode. (d) HRTEM image corresponding to the area marked with a yellow rectangle in (c). (e) STEM image of as-prepared FeP film. (f) EDX line profiles of FeP film taken along the path marked in (e).

which is close to the expected 1:1 FeP stoichiometry, as well as to the results of inductively coupled plasma (ICP) measurements (44% Fe and 56% P, Fig. S5 in the ESM). More detailed structural information on the FeP nanopetals can be obtained by the transmission electron microscopy (TEM) analysis in Fig. 3(c) and Fig. S6 in the ESM. A high-resolution TEM (HRTEM) image of a selected area from a single nanopetal displays well-resolved lattice fringes (Fig. 3(d)). The measured interplanar spacings of 0.273 and 0.259 nm match well with those of the (011) and (200) crystal planes of FeP. A closer inspection of the figure reveals crystallized FeP surrounded by amorphous regions (indicated by yellow circles), in good agreement with the XRD results. According to previous studies, this interesting structure is expected to result in a more efficient HER performance [33, 34]. In addition, the scanning TEM (STEM) image in Fig. 3(e) clearly reveals the 3D structure of the film. Finally, the corresponding EDX line profiles further confirm the uniform distribution of Fe and P elements throughout the film (Fig. 3(f)).

The surface composition and oxidation states of the as-prepared FeO(OH) and FeP films were further examined by X-ray photoelectron spectroscopy (XPS). For the FeO(OH) film, the Fe $2p_{3/2}$ and Fe $2p_{1/2}$ core level peaks are observed at binding energies of 710.2 and 724.0 eV, respectively, together with satellite features (Fig. 4(a)), in agreement with literature data for α-FeO(OH) [35]. The O 1s core level spectrum can also be deconvoluted into two peaks at 530.4 and 529.0 eV (Fig. 4(b)). The former peak corresponds to the absorption of oxygen or water molecules on the surface of the composite, while the second one results from O_2-forming oxide with Fe elements [35]. After the phosphorization reaction at 350 °C, the Fe 2p core level spectrum shifts to higher binding energies, together with the appearance of a minor peak at a lower binding energy of 707.5 eV, which could be assigned to FeP, in good agreement with previous reports (Fig. 4(c)) [36]. The corresponding P 2p region displays two peak regions (Fig. 4(d)), one centered at binding energies of 129.5 and 130.1 eV (P $2p_{3/2}$ and P $2p_{1/2}$), characteristic of phosphorus in FeP [36], and another peak at 133.6 eV. Together with the shifted Fe core level peaks, the latter can be assigned to oxidized

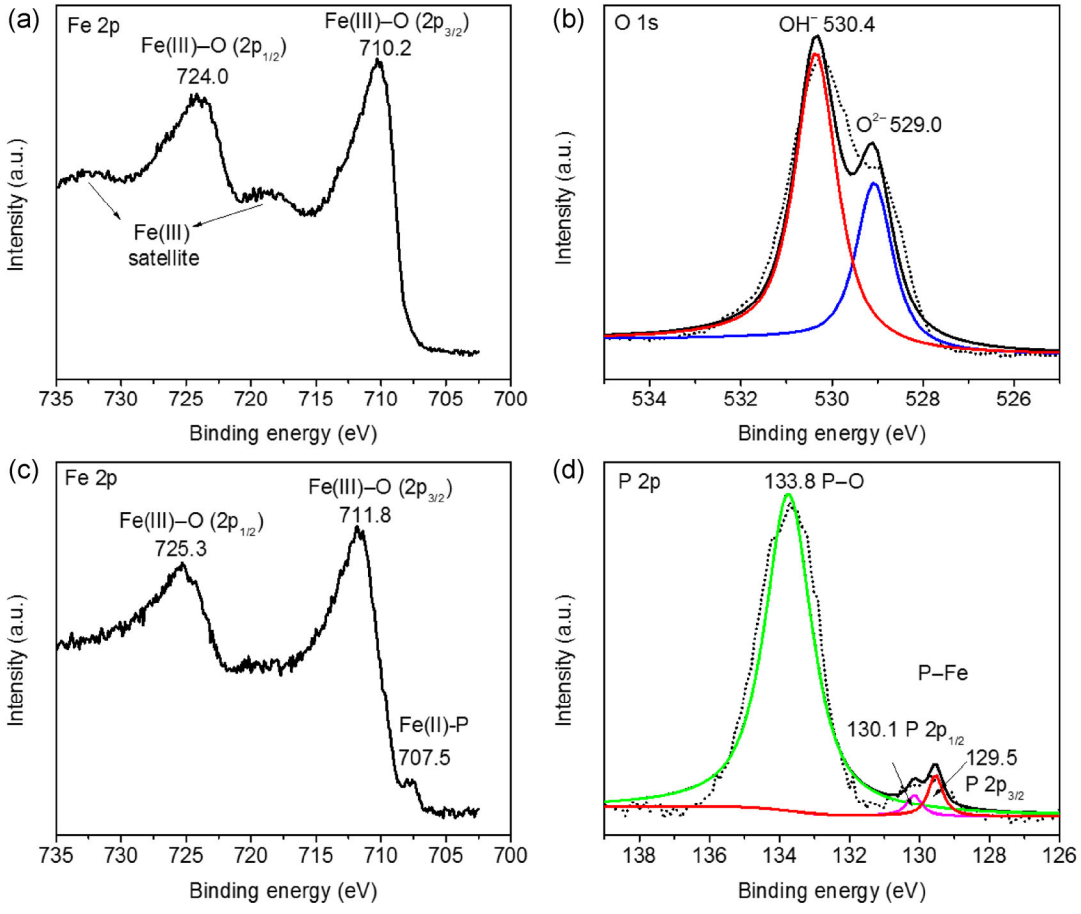

Figure 4 Fe 2p (a) and O 1s (b) XPS spectra of FeO(OH) film precursor; Fe 2p (c) and P 2p (d) XPS spectra of hierarchical FeP film.

P and Fe species in FeP, which could be due to surface oxidation in the atmosphere, as often observed for transition metal phosphide materials [37]. In addition, in-depth XPS analysis indicates that after 5 min of Ar^+ etching the peaks corresponding to oxidized Fe and P species decrease, while the FeP peaks increase. On the other hand, only the FeP peaks are observed after 10 min etching, suggesting a homogeneous distribution of the component elements inside the film and the complete chemical conversion of FeO(OH) into FeP (Fig. S7 in the ESM).

2.2 Electrochemical measurements

It is well known that the electrochemical performance of an electrode strongly depends not only on the intrinsic crystalline structure and on the surface composition of the active catalysts, but also on the morphology and assembled structure of the active composites. In the case of the nanostructured FeP array film, the uniquely oriented FeP nanopetals are expected to reduce the adhesion and accelerate the release of the hydrogen gas formed, as well as maximizing the exposure of the reactive edges to the liquid electrolyte, so as to accelerate electron/proton transfer or diffusion [18, 38]. At the same time, the high intrinsic activity and conductivity of FeP also improves the efficiency of the HER process [39]. Furthermore, the mixture of amorphous and crystalline phases in the as-received FeP is also expected to be beneficial for the HER due to the higher number of exposed active sites compared with the highly crystalline FeP [40]. Having obtained a sufficient understanding of the structure and composition of the FeP film electrode, we turned to assess the HER performance of the film in H_2-saturated electrolytes over a wide pH range. As the concentration of glycerol has a certain effect on the morphology of the resulting FeP films, we first investigated the HER activity of the

FeP films obtained with different glycerol amounts (Fig. S8 in the ESM). The FeP film obtained with a glycerol/water volume ratio of 1:3 showed the highest HER activity in both conditions, but only slightly higher than that of the FeP film prepared with 1:7 volume ratio, which could be due to the similar morphology of the two films. On the other hand, the FeP film with 1:1 ratio needed the largest overpotential to reach the same current density; this could be due to the lower number of active sites per area in the film, as the FeP nanopetals grew only on one side of the film. Therefore, the FeP film with 1:3 water/glycerol ratio was selected for further electrochemical characterization.

Figure 5(a) shows the polarization curves obtained for representative FeP film electrodes, along with the results obtained under identical conditions for bare Ti foil (after phosphorization at 350 °C) and commercial Pt/C electrodes. As expected, the Ti foil electrode is HER-inactive under such conditions. After evaluating the resistance, an *i*R correction was applied to the electrochemical measurements (Fig. S9 in the ESM). Note that all electrodes were tested in a static state without rotation, to mimic real industrial operation. A rapid cathodic current increase was observed in 0.5 M H_2SO_4 for the nanostructured FeP film below −25 mV vs. reversible hydrogen electrode (RHE); further scanning towards more negative potentials gave rise to a dramatic increase in current density, which even exceeded that of Pt/C at potentials below −158 mV vs. RHE (Fig. 5(a)). The onset overpotential (determined from the recorded linear sweep voltammetry (LSV) curves based on a current density of 1 mA·cm^{-2}) of the FeP film electrode was estimated to be ~ 16 mV, and an overpotential of only 65 mV was required to drive a kinetic current density of 10 mA·cm^{-2}. These overpotentials compare favorably with the performance of most reported metal phosphides HER catalysts in acidic conditions (Table S1 in the ESM). The inset of Fig. 5(a) displays the Tafel slopes obtained for all samples. A slope of 30 mV·dec^{-1} was obtained for commercial Pt/C in an acidic electrolyte, consistent with the reported values for the Pt-catalyzed HER [41]. By contrast, the Tafel slope of the FeP film electrode was 48.5 mV·dec^{-1}, indicating that different HER mechanisms are active on the FeP nanostructure array film and Pt. The behavior of FeP is consistent with the combined Volmer-Heyrovsky

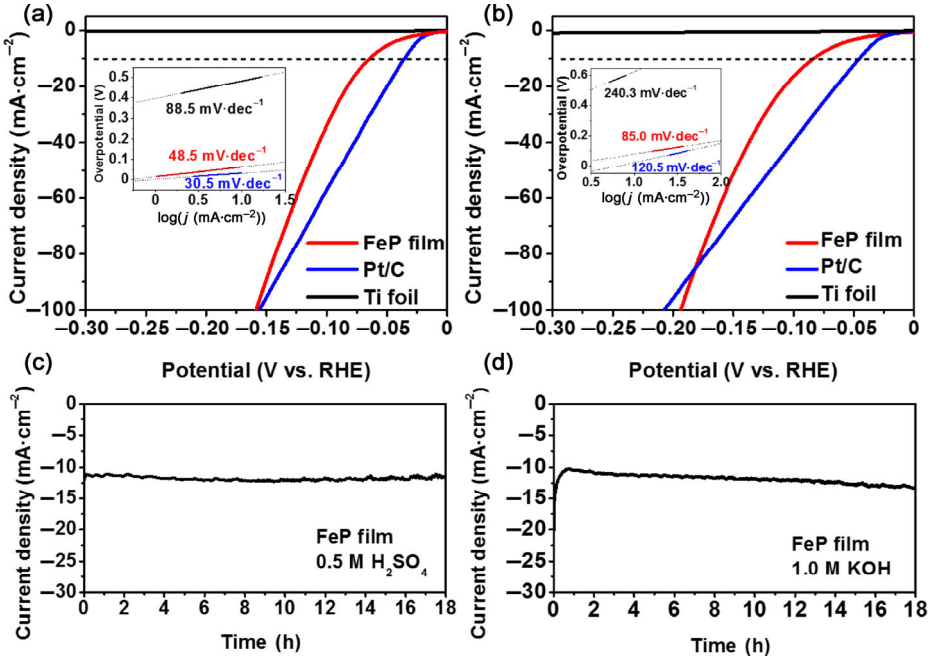

Figure 5 (a) and (b) Polarization curves measured in 0.5 M H_2SO_4 (a) and 1.0 M KOH (b) with a scan rate of 5 mV·s^{-1}. The insets show the corresponding Tafel plots. (c) and (d) Stability tests for FeP film electrode at a static overpotential of 100 mV in 0.5 M H_2SO_4 (c) and 120 mV in 1.0 M KOH (d) for 18 h.

mechanism, in which the bond strength of the adsorbed hydrogen is strong enough to provide a sufficient coverage of the intermediate, but not enough to desorb the product [42]. Similar Tafel slopes have been previously reported for other transition metal-based phosphides, such as MoP (56 mV·dec^{-1}) [43], CoP (50 mV·dec^{-1}) [44], and Ni_2P (46 mV·dec^{-1}) [45]. As mentioned above, the as-obtained FeP film contains an amorphous phase; hence, a control experiment was conducted to investigate the influence of such structure on the HER activity. The results show that when the phosphorization temperature was increased to 450 ˚C, the obtained FeP film exhibited high crystallinity (Figs. S10(a) and S10(b) in the ESM), but much lower HER activity compared with the present FeP film electrode (Fig. S10(c) in the ESM). Figure S11 in the ESM shows the polarization curves normalized by the number of active sites, expressed in term of the turnover frequency (TOF). The TOF value of the as-received FeP film was estimated to be 1.55 s^{-1} in 0.5 M H_2SO_4 at the overpotential of 200 mV, which is much higher than the values obtained for Ni_2P/Ti (0.725 s^{-1} at 205 mV) [46] and defect-rich MoS_2 (0.725 s^{-1} at 300 mV) [47].

Remarkably, the onset overpotential of the FeP nanostructured film in an alkaline electrolyte was as low as 16 mV, and an overpotential of only 84 mV was required to achieve a geometric current density of 10 mA·cm^{-2} (Fig. 5(b)). At a potential of −193 mV vs. RHE, the FeP film can generate a catalytic current density of 100 mA·cm^{-2}, which even exceeds that of the commercial Pt/C electrocatalyst. These overpotentials are comparable to, or even exceed, those of most reported Pt-free HER catalysts in alkaline media (Table S2 in the ESM). Moreover, the corresponding Tafel plots yield a much smaller slope of 85.0 mV·dec^{-1} compared with Pt/C (120.5 mV·dec^{-1}), further confirming the favorable electrochemical kinetics for the HER process (inset of Fig. 5(b)). The HER reaction on the FeP film in acidic conditions was shown to proceed through the Volmer-Heyrovsky mechanism. Durst et al. suggested that the mechanism does not change in a strong base, except that the Heyrovsky or Volmer step is followed by rapid recombination between H^+ cations and the abundant OH^- anions of the alkaline electrolytes [48], and thus the hydrogen binding energy is the dominating factor controlling the HER in both strong acids and strong bases. This hypothesis was confirmed by the density functional theory (DFT) calculations performed in this work.

The stability performance of the FeP film electrodes was then investigated by long-term cycling and chronoamperometry electrolysis experiments at overpotentials of 100 and 120 mV in acidic and alkaline electrolytes, respectively, for 18 h. After 5,000 continuous cyclic voltammetry (CV) cycles, the nanostructured FeP film electrodes still showed steady performances in either 0.5 M H_2SO_4 or 1.0 M KOH, as indicated by the smooth curves recorded, with only slight current degradation (Fig. S12 in the ESM). Figures 5(c) and 5(d) show the chronoamperometry plots; the FeP array film exhibited excellent long-term stability at the measured overpotential under both conditions. The durability of the present systems exceeds that of other reported FeP-based HER electrocatalysts, especially in basic conditions [12, 14]. The FeP films mostly retained their initial morphology after the stability tests; however, the nanopetals were packed closely together after long-term HER (Fig. S13 in the ESM). Faradaic efficiency tests of the HER process in acidic and basic media were conducted at a constant applied potential for 120 min, and showed a near 100% Faradaic efficiency (Fig. S14 in the ESM). It should be noticed that the FeP film electrode also performed well in neutral solution. Figure S15 in the ESM shows the polarization curves for the FeP film electrode before and after 2,000 CV cycles at a scan rate of 50 mV·s^{-1} in 1.0 M phosphate buffer solution (PBS, pH 7), showing a Tafel slope of 69.4 mV·dec^{-1} and no measurable loss of catalytic activity.

Except for the advantages of the intrinsic crystalline structure of FeP, the excellent performance of the present materials can be rationalized in terms of the electrode design. The vertical FeP nanopetal arrays with porous structure could significantly improve the release rate of H_2 gas generated at the electrode surface during the HER process, which effectively prevent the accumulation of the H_2 gas bubbles on the catalyst surface and thus lead to a better long-term stability [17, 18]. To confirm this hypothesis, we

prepared a FeP plate electrode and assessed its HER activity; the electrode showed a much lower HER activity than the FeP film electrode, demonstrating the significant role of the FeP morphology on the HER performance (Fig. S16 in the ESM). In the current study, the FeP film electrode was obtained by supporting the film on Ti foil; however, alternative architectures can be produced, for example, by directly attaching the FeP film catalysts onto the cathode of a water-splitting cell to form an integrated system.

2.3 Density functional theory calculations

To understand the basis of the catalytic activity of the hierarchical FeP array film, the Gibbs free energy (ΔG^0_H) was used as descriptor to evaluate the catalysts using DFT calculations (additional computational details can be found in the ESM). For an ideal HER catalyst, ΔG^0_H should be close to zero ($|\Delta G^0_H| \rightarrow 0$) [49]. In order to select a suitable surface to perform the calculations, we calculated the free energies of low-index surfaces with different terminations, and used them to measure the corresponding stability. Among all the surfaces considered, the mixed P/Fe-terminated FeP(011) surface (FeP(011)-$T_{P/Fe}$) exhibited the lowest surface free energy (Table S3 and Fig. S17 in the ESM), which is consistent with our experimental data (Fig. 3(d)). Thus, the mixed P/Fe termination of the FeP(011) surface was chosen to study H adsorption (Fig. S18 in the ESM). As shown in Fig. 6, when the H coverage reaches 1/4 of a monolayer (ML, defined as one hydrogen adsorbed on a 2 × 2 slab), the ΔG^0_H calculated for FeP(011)-$T_{P/Fe}$ was 0.09 eV, fulfilling the $|\Delta G^0_H| \rightarrow 0$ requirement. The $|\Delta G^0_H|$ value of FeP(011)-$T_{P/Fe}$ is smaller than those reported for MoP(001) (−0.36 eV) [43] and Pt(111) (−0.41 eV) [50]. This highlights a higher hydrogen evolution activity for FeP(011)-$T_{P/Fe}$ compared with P-terminated MoP(001) at lower coverage, consistent with experimental results [43]. Further increasing the coverage from 1/4 ML to 1 ML, the $|\Delta G^0_H|$ value of FeP(011)-$T_{P/Fe}$ remained the smallest, with only a small change from 0.09 to −0.11 eV (Fig. S19 and Table S4 in the ESM), indicating a weaker coverage dependence of the free energy of the mixed P/Fe termination compared to that of MoP(001) (which increased from −0.36 to 0.54 eV) [43]. Whereas these findings may provide useful insight for the development of metal phosphides for the HER process, future work focused on the FeP surface would be required to fully understand the phenomena involved.

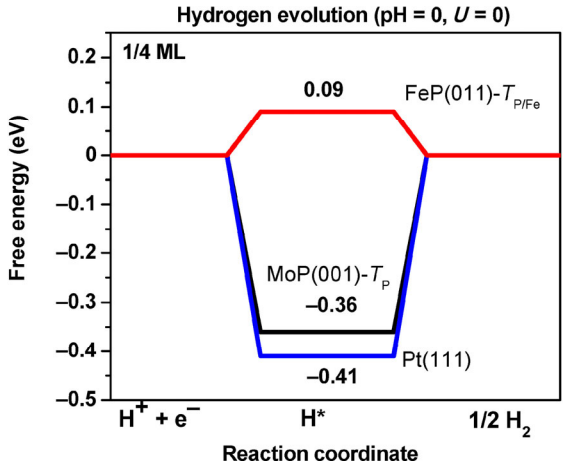

Figure 6 Schematic energy profiles for the HER process on the mixed P/Fe termination ($T_{P/Fe}$) of FeP(011), the P termination (T_P) of MoP(001), and Pt(111). The data for MoP [43] and Pt(111) [50] were obtained using the VASP code and the Perdew–Burke–Ernzerhof (PBE) functional. The H coverage is 1/4 ML for each catalyst. Note that the ΔG^0_H value barely changes at lower coverages, due to the weak interaction between the adsorbate and the surface.

3 Conclusions

In conclusion, this work presents a bio-inspired strategy for the synthesis of hierarchical FeP nanostructure array films, based on the morphology-preserving thermal transformation of film-shaped FeO(OH) nanostructures. The nanostructured FeP array film can be used as gas-evolving electrode for the HER over a wide pH range electrolytes. DFT calculations show that the mixed P/Fe surface terminations likely represent the active catalytic sites, achieving a Gibbs free energy close to zero. Due to their excellent HER performance, the hierarchical FeP films represent a promising alternative to platinum as HER electrodes, with great potential for application in hydrogen production by water splitting technologies. More importantly, the present bio-inspired synthetic approach bridges the gap between biological and inorganic self-assembling nanosystems and opens up a new avenue for the rational design of functional

nanostructures for electrochemical reactions and energy devices based on gas generation.

Acknowledgements

This project is funded by the Program for Associate Professor of Special Appointment (Young Eastern Scholar) at Shanghai Institutions of Higher Learning (No. QD2016013), the Natural Science Foundation of Shanghai (No. 16ZR1423500) and the National Natural Science Foundation of China (No. 51702213). We also acknowledge financial support by the National 1000 Young Talents Program of China, the Innovation Foundation of Shenzhen Government (No. JCYJ20160408173202143), the Joint Fund of Energy Storage of Qingdao (No. 20160012), the Fundamental Research Funds for the Central Universities (No. 2017KFXKJC002) and the Innovation Research Funds of HUST (No. 2017KFYXJJ164). The Program Sponsored by Shanghai Pujiang (No. 17PJ1406900) is also acknowledged. We also acknowledge the support of the Analytical and Testing Center of Huazhong University of Science and Technology for XRD, TEM, and XPS measurements.

Electronic Supplementary Material: Supplementary material (experimental details, DFT calculation, XRD, EDX, SEM, TEM, and other electrochemical results) is available in the online version of the article at https://doi.org/10.1007/s12274-017-1919-2.

References

[1] Dunn, S. Hydrogen futures: Toward a sustainable energy system. *Int. J. Hydrogen Energy* **2002**, *27*, 235–264.

[2] Jiao, Y.; Zheng, Y.; Jaroniec, M.; Qiao, S. Z. Design of electrocatalysts for oxygen- and hydrogen-involving energy conversion reactions. *Chem. Soc. Rev.* **2015**, *44*, 2060–2086.

[3] Zou, X. X.; Zhang, Y. Noble metal-free hydrogen evolution catalysts for water splitting. *Chem. Soc. Rev.* **2015**, *44*, 5148–5180.

[4] Jiao, L.; Zhou, Y. X.; Jiang, H. L. Metal-organic framework-based CoP/reduced graphene oxide: High-performance bifunctional electrocatalyst for overall water splitting. *Chem. Sci.* **2016**, *7*, 1690–1695.

[5] You, B.; Jiang, N.; Liu, X.; Sun, Y. J. Simultaneous H_2 generation and biomass upgrading in water by an efficient noble-metal-free bifunctional electrocatalyst. *Angew. Chem., Int. Ed.* **2016**, *55*, 9913–9917.

[6] You, B.; Liu, X.; Jiang, N.; Sun, Y. J. A general strategy for decoupled hydrogen production from water splitting by integrating oxidative biomass valorization. *J. Am. Chem. Soc* **2016**, *138*, 13639–13646.

[7] Pu, Z. H.; Wei, S. Y.; Chen, Z. B.; Mu, S. C. Flexible molybdenum phosphide nanosheet array electrodes for hydrogen evolution reaction in a wide ph range. *Appl. Catal. B* **2016**, *196*, 193–198.

[8] Miao, M.; Pan, J.; He, T.; Yan, Y.; Xia, B. Y.; Wang, X. Molybdenum carbide-based electrocatalysts for hydrogen evolution reaction. *Chem.-Eur. J.* **2017**, *23*, 10947–10961.

[9] Li, D. Q.; Liao, Q. Y.; Ren, B. W.; Jin, Q. Y.; Cui, H.; Wang, C. X. A 3D-composite structure of FEP nanorods supported by vertically aligned graphene for the high-performance hydrogen evolution reaction. *J. Mater. Chem. A* **2017**, *5*, 11301–11308.

[10] Ren, B. W.; Li, D. Q.; Jin, Q. Y.; Cui, H.; Wang, C. X. Novel porous tungsten carbide hybrid nanowires on carbon cloth for high-performance hydrogen evolution. *J. Mater. Chem. A* **2017**, *5*, 13196–13203.

[11] Wang, H.; Min, S. X.; Wang, Q.; Li, D. B.; Casillas, G.; Ma, C.; Li, Y. Y.; Liu, Z. X.; Li, L. J.; Yuan, J. Y. et al. Nitrogen-doped nanoporous carbon membranes with Co/CoP janus-type nanocrystals as hydrogen evolution electrode in both acidic and alkaline environments. *ACS Nano* **2017**, *11*, 4358–4364.

[12] Jiang, P.; Liu, Q.; Liang, Y. H.; Tian, J. Q.; Asiri, A. M.; Sun, X. P. A cost-effective 3D hydrogen evolution cathode with high catalytic activity: FeP nanowire array as the active phase. *Angew. Chem., Int. Ed.* **2014**, *53*, 12855–12859.

[13] Shi, Y. M.; Zhang, B. Recent advances in transition metal phosphide nanomaterials: Synthesis and applications in hydrogen evolution reaction. *Chem. Soc. Rev.* **2016**, *45*, 1529–1541.

[14] Liang, Y. H.; Liu, Q.; Asiri, A. M.; Sun, X. P.; Luo, Y. L. Self-supported FeP nanorod arrays: A cost-effective 3D hydrogen evolution cathode with high catalytic activity. *ACS Catal.* **2014**, *4*, 4065–4069.

[15] Zhang, Z.; Lu, B. P.; Hao, J. H.; Yang, W. S.; Tang, J. L. FeP nanoparticles grown on graphene sheets as highly active non-precious-metal electrocatalysts for hydrogen evolution reaction. *Chem. Commun.* **2014**, *50*, 11554–11557.

[16] Tian, J. Q.; Liu, Q.; Liang, Y. H.; Xing, Z. C.; Asiri, A. M.; Sun, X. P. FeP nanoparticles film grown on carbon cloth: An ultrahighly active 3D hydrogen evolution cathode in both acidic and neutral solutions. *ACS Appl. Mater. Interfaces* **2014**, *6*, 20579–20584.

[17] Lu, Z. Y.; Zhu, W.; Yu, X. Y.; Zhang, H. C.; Li, Y. J.; Sun, X. M.; Wang, X. W.; Wang, H.; Wang, J. M.; Luo, J. et al. Ultrahigh hydrogen evolution performance of under-water "superaerophobic" MoS_2 nanostructured electrodes. *Adv. Mater.* **2014**, *26*, 2683–2687.

[18] Lu, Z. Y.; Li, Y. J.; Lei, X. D.; Liu, J. F.; Sun, X. M. Nanoarray based "superaerophobic" surfaces for gas evolution reaction electrodes. *Mater. Horiz.* **2015**, *2*, 294–298.

[19] Meldrum, F. C.; Cölfen, H. Controlling mineral morphologies and structures in biological and synthetic systems. *Chem. Rev.* **2008**, *108*, 4332–4432.

[20] Wang, B.; Chen, J. S.; Lou, X. W. The comparative lithium storage properties of urchin-like hematite spheres: Hollow vs. solid. *J. Mater. Chem. A* **2012**, *22*, 9466–9468.

[21] Wei, Z. H.; Xing, R. G.; Zhang, X.; Liu, S.; Yu, H. H.; Li, P. C. Facile template-free fabrication of hollow nestlike α-Fe_2O_3 nanostructures for water treatment. *ACS Appl. Mater. Interfaces* **2013**, *5*, 598–604.

[22] Mayer, G. Rigid biological systems as models for synthetic composites. *Science* **2005**, *310*, 1144–1147.

[23] Oaki, Y.; Kajiyama, S.; Nishimura, T.; Kato, T. Selective synthesis and thin-film formation of α-cobalt hydroxide through an approach inspired by biomineralization. *J. Mater. Chem.* **2008**, *18*, 4140–4142.

[24] Uchiyama, H.; Hosono, E.; Zhou, H. S.; Imai, H. Three-dimensional architectures of spinel-type $LiMn_2O_4$ prepared from biomimetic porous carbonates and their application to a cathode for lithium-ion batteries. *J. Mater. Chem.* **2009**, *19*, 4012–4016.

[25] Kokubu, T.; Oaki, Y.; Uchiyama, H.; Hosono, E.; Zhou, H. S.; Imai, H. Biomimetic synthesis of metal ion-doped hierarchical crystals using a gel matrix: Formation of cobalt-doped $LiMn_2O_4$ with improved electrochemical properties through a cobalt-doped $MnCo_3$ precursor. *Chem. Asian J.* **2010**, *5*, 792–798.

[26] Liu, L.; Yang, L. Q.; Liang, H. W.; Cong, H. P.; Jiang, J.; Yu, S. H. Bio-inspired fabrication of hierarchical feooh nanostructure array films at the air–water interface, their hydrophobicity and application for water treatment. *ACS Nano* **2013**, *7*, 1368–1378.

[27] Guo, X. H.; Yu, S. H.; Cai, G. B. Crystallization in a mixture of solvents by using a crystal modifier: Morphology control in the synthesis of highly monodisperse $CaCo_3$ microspheres. *Angew. Chem., Int. Ed.* **2006**, *118*, 4081–4085.

[28] Chen, S. F.; Zhu, J. H.; Jiang, J.; Cai, G. B.; Yu, S. H. Polymer-controlled crystallization of unique mineral superstructures. *Adv. Mater.* **2010**, *22*, 540–545.

[29] McCusker, L. B. Product characterization by X-ray powder diffraction. *Microporous Mesoporous Mater.* **1998**, *22*, 527–529.

[30] Li, J. T.; Zhao, W.; Huang, F. Q.; Manivannan, A.; Wu, N. Q. Single-crystalline $Ni(OH)_2$ and NiO nanoplatelet arrays as supercapacitor electrodes. *Nanoscale* **2011**, *3*, 5103–5109.

[31] Amano, F.; Li, D.; Ohtani, B. Fabrication and photoelectrochemical property of tungsten(VI) oxide films with a flake-wall structure. *Chem. Commun.* **2010**, *46*, 2769–2771.

[32] Guo, X.; Zhang, F.; Xu, S.; Evans, D. G.; Duan, X. Preparation of layered double hydroxide films with different orientations on the opposite sides of a glass substrate by *in situ* hydrothermal crystallization. *Chem. Commun.* **2009**, 6836–6838.

[33] Paseka, I.; Velicka, J. Hydrogen evolution and hydrogen sorption on amorphous smooth MeP(X) (Me = Ni, Co and FeNi) electrodes. *Electrochim. Acta* **1997**, *42*, 237–242.

[34] Paseka, I. Influence of hydrogen absorption in amorphous Ni–P electrodes on double layer capacitance and charge transfer coefficient of hydrogen evolution reaction. *Electrochim. Acta* **1999**, *44*, 4551–4558.

[35] Abdel-Samad, H.; Watson, P. R. An XPS study of the adsorption of chromate on goethite (α-FeOOH). *Appl. Surf. Sci.* **1997**, *108*, 371–377.

[36] Qian, C.; Kim, F.; Ma, L.; Tsui, F.; Yang, P. D.; Liu, J. Solution-phase synthesis of single-crystalline iron phosphide nanorods/nanowires. *J. Am. Chem. Soc.* **2004**, *126*, 1195–1198.

[37] Yan, Y.; Xia, B. Y.; Ge, X. M.; Liu, Z. L.; Fisher, A.; Wang, X. A flexible electrode based on iron phosphide nanotubes for overall water splitting. *Chem.-Eur. J.* **2015**, *21*, 18062–18067.

[38] Faber, M. S.; Dziedzic, R.; Lukowski, M. A.; Kaiser, N. S.; Ding, Q.; Jin, S. High-performance electrocatalysis using metallic cobalt pyrite (CoS_2) micro- and nanostructures. *J. Am. Chem. Soc.* **2014**, *136*, 10053–10061.

[39] Oyama, S. T.; Gott, T.; Zhao, H. Y.; Lee, Y. K. Transition metal phosphide hydroprocessing catalysts: A review. *Catal. Today* **2009**, *143*, 94–107.

[40] Masa, J.; Weide, P.; Peeters, D.; Sinev, I.; Xia, W.; Sun, Z. Y.; Somsen, C.; Muhler, M.; Schuhmann, W. Amorphous cobalt boride (Co_2B) as a highly efficient nonprecious catalyst for electrochemical water splitting: Oxygen and hydrogen evolution. *Adv. Energy Mater.* **2016**, *6*, 1502313.

[41] Laursen, A. B.; Patraju, K. R.; Whitaker, M. J.; Retuerto, M.; Sarkar, T.; Yao, N.; Ramanujachary, K. V.; Greenblatt, M.; Dismukes, G. C. Nanocrystalline Ni_5P_4: A hydrogen evolution electrocatalyst of exceptional efficiency in both alkaline and acidic media. *Energy Environ. Sci.* **2015**, *8*, 1027–1034.

[42] Lasia, A. Hydrogen Evolution Reaction. *Handbook of Fuel Cells* **2010**.

[43] Xiao, P.; Sk, M. A.; Thia, L.; Ge, X. M.; Lim, R. J.; Wang, J. Y.; Lim, K. H.; Wang, X. Molybdenum phosphide as an efficient electrocatalyst for the hydrogen evolution reaction. *Energy Environ. Sci.* **2014**, *7*, 2624–2629.

[44] Popczun, E. J.; Read, C. G.; Roske, C. W.; Lewis, N. S.; Schaak, R. E. Highly active electrocatalysis of the hydrogen evolution reaction by cobalt phosphide nanoparticles. *Angew. Chem., Int. Ed.* **2014**, *126*, 5531–5534.

[45] Popczun, E. J.; McKone, J. R.; Read, C. G.; Biacchi, A. J.; Wiltrout, A. M.; Lewis, N. S.; Schaak, R. E. Nanostructured nickel phosphide as an electrocatalyst for the hydrogen evolution reaction. *J. Am. Chem. Soc.* **2013**, *135*, 9267–9270.

[46] Pu, Z. H.; Liu, Q.; Tang, C.; Asiri, A. M.; Sun, X. P. Ni_2P nanoparticle films supported on a Ti plate as an efficient hydrogen evolution cathode. *Nanoscale* **2014**, *6*, 11031–11034.

[47] Xie, J. F.; Zhang, H.; Li, S.; Wang, R. X.; Sun, X.; Zhou, M.; Zhou, J. F.; Lou, X. W.; Xie, Y. Defect-rich MoS_2 ultrathin nanosheets with additional active edge sites for enhanced electrocatalytic hydrogen evolution. *Adv. Mater.* **2013**, *25*, 5807–5813.

[48] Durst, J.; Siebel, A.; Simon, C.; Hasché, F.; Herranz, J.; Gasteiger, H. A. New insights into the electrochemical hydrogen oxidation and evolution reaction mechanism. *Energy Environ. Sci.* **2014**, *7*, 2255–2260.

[49] Hinnemann, B.; Moses, P. G.; Bonde, J.; Jørgensen, K. P.; Nielsen, J. H.; Horch, S.; Chorkendorff, I.; Nørskov, J. K. Biomimetic hydrogen evolution: MoS_2 nanoparticles as catalyst for hydrogen evolution. *J. Am. Chem. Soc.* **2005**, *127*, 5308–5309.

[50] Hanh, T. T. T.; Takimoto, Y.; Sugino, O. First-principles thermodynamic description of hydrogen electroadsorption on the Pt(111) surface. *Surf. Sci.* **2014**, *625*, 104–111.